International Journal of Applied Earth Observation and Geoinformation 129 (2024) 103806

Contents lists available at ScienceDirect

International Journal of Applied Earth Observation and Geoinformation

journal homepage: www.elsevier.com/locate/jag

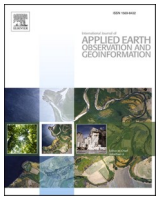

The unsuPervised shAllow laNdslide rapiD mApping: PANDA method applied to severe rainfalls in northeastern appenine (Italy)

Davide Notti, Martina Cignetti *, Danilo Godone, Davide Cardone, Daniele Giordan

National Research Council of Italy, Research Institute for Geo-Hydrological Protection (CNR IRPI), Torino 10135, Italy

ARTICLE INFO

Keywords:
Semi-automatic processing
Sentinel-2
Extreme event
Emergency management
Residual risk
Change detection
Emilia-Romagna Region

ABSTRACT

Shallow landslides, frequently triggered by extreme events such as heavy rainfall, snowmelt, or earthquakes, affect vast areas with remarkable density. In the immediate aftermath of such events, it becomes crucial to rapidly assess landslides distribution and pinpoint the most severely affected areas to prioritize damage assessments and guide field survey operations effectively. Once the emergency phase subsides, the attention can shift to enhancing the accuracy of landslide inventory. In this work, we introduce the two-phase methodology "PANDA", the unsuPervised shAllow laNdslide rapiD mApping, for the low-cost mapping of the potential landslides, firstly in the emergency phase and then, with an improved version, in the post-emergency one. This approach utilizes variations in NDVI derived from Sentinel-2 satellite imagery and geomorphological filters. We applied PANDA to rainfall events in the northeastern Apennine range, Italy, occurred in May 2023, causing dramatic social and economic consequences for this mountain territory. Within just five days of obtaining Sentinel-2 post-event imagery, we produced a reliable, ready-to-use map covering a vast area (~4000 km^2). The map tested during emergency field mapping shows positive feedback. In the post-emergency phase, accuracy was enhanced using completely cloud-free imagery, a filter to identify false positives associated with land use changes, a higher resolution digital terrain model (DTM), and an iterative approach to optimize NDVI and slope thresholds. Potential landslide density related with rainfall, indicating that the most severely affected region attained a density of approximately 50 landslides/km^2. Validation against an independent manual inventory based on high-resolution imagery demonstrated encouraging accuracy results from both inventories, with a noticeable increase in the F1 score for the post-emergency version.

1. Introduction

Extreme rainfall events are one of the primary triggers of shallow landslides (Guzzetti et al., 2008). They usually initiate almost simultaneously, densely distributed and involving large territory (Bessette-Kirton et al., 1950; Cignetti et al., 2019; Guzzetti et al., 2004), causing severe damage, especially, to the road network (Bordoni et al., 2018; Giordan et al., 2017). After those events, one of the first activities necessary to evaluate the damage is a rapid mapping of landslides. Landslide event inventory mapping is one of the main approaches to estimating the level of risk posed by geo-hydrological hazards, playing a crucial role in recording the date of triggered events and evaluating the spatial extent and the magnitude of landslides (Corominas et al., 2014; Guzzetti et al., 2005; van Westen et al., 2008). Many approaches have been proposed for landslide event inventory mapping (Novellino et al., 2024). Traditional methods rely on 3D visual interpretation of aerial photos or satellite images, coupled with extensive field surveys (Brardinoni et al., 2003; Santangelo et al., 2015). The increased availability of high-resolution images (from Unmanned Aerial Vehicle (UAV), aerial or satellite platforms) (Casagli et al., 2017; Giordan et al., 2020) allowed accurate mapping of small landslides. Unfortunately, these products are rarely free-cost and require an acquisition plan and/or only cover some of the area affected. Moreover, detailed mapping needs a time-consuming expert manual approach (Donnini et al., 2023; Guzzetti et al., 2012) or the development of a machine learning algorithm that requires a high level of expertise (Đurić et al., 2017; Galli et al., 2008; Lu et al., 2019; Meena et al., 2023; Murillo-García et al., 2015). The advent of remote sensing technologies has opened opportunities for the development of methodologies and techniques for automating landslides mapping through the utilization of various high-resolution optical

* Corresponding author.
E-mail addresses: davide.notti@irpi.cnr.it (D. Notti), martina.cignetti@irpi.cnr.it (M. Cignetti), danilo.godone@irpi.cnr.it (D. Godone), davide.cardone@irpi.cnr.it (D. Cardone), daniele.giordan@irpi.cnr.it (D. Giordan).

https://doi.org/10.1016/j.jag.2024.103806
Received 19 January 2024; Received in revised form 18 March 2024; Accepted 29 March 2024
Available online 5 April 2024

sensor products, significantly reducing the timing for the mapping (Casagli et al., 2016; Guzzetti et al., 2012). Recent studies (Nava et al., 2022; Santangelo et al., 2022) use also the amplitude of Synthetic Aperture Radar (SAR) derived products to overcome the problem of cloud cover of multi-spectral satellite data. However, SAR techniques introduce some other limitations (*e.g.*, vegetation and snow coverage, shawdowing, decorrelation noise), necessitating the expertise of users to process the data.

The Sentinel-2 satellites, with a 5-day revisiting pass, allow medium-resolution images over wide areas and the possibility to compare the post-event images with the same condition of sunlight direction angle (Drusch et al., 2012). The availability of these images allows a rapid, fully or partially, automatic mapping of potential landslides (PL) over vast areas as soon as cloud-free images are available using the variation of NDVI (Ghorbanzadeh et al., 2022b; Notti et al., 2023b). These maps aim to estimate the severity of the event and its impact, and to focus the high-resolution mapping on the most affected areas.

Despite NDVI-based landslide mapping methods offering rapid results, and low computational and economic costs, ensuring a user-friendly approach even for non-expert users, diverse drawbacks need to be taken into account. Final products may be influenced by shadowed areas, cloud coverage, NDVI variations associated with agricultural activities and deforestation, as well as river erosional processes, potentially leading to an increased number of false positives in the mapped results. In recent years, various methods that aim to solve the limitation related to the use of NDVI images have emerged from different researchers. Fiorucci et al., (2019) proposed a manual mapping approach that leverages NDVI images coupled with digital stereoscopy for the 3D visualization of landslide events mapping, even in shadowed areas. Other authors have developed algorithms that exploit the slow regrowth of vegetation in landslide detachment areas to automatically detect landslides using NDVI time series data following the triggering event. However, this approach faces challenges with cloud coverage, making it unsuitable for rapid landslide mapping after a catastrophic event (Milledge et al., 2022). The recent advancement of new machine learning techniques, in particular, the algorithms that use the convolutional Neural Network (CNN) and Fully Convolutional Network (FCN) for image segmentation (Ghorbanzadeh et al., 2021), has facilitated the analysis of extensive datasets, enabling the observation of NDVI trends over extended periods and facilitating the identification of various factors influencing these fluctuations, such as seasonality, landslide triggers, and human activities (Doan et al., 2023).This work presents a two-phase methodology aimed at the low-cost mapping of shallow landslides: the unsuPervised shAllow laNdslide rapiD mApping - PANDA method. The first step (PANDA-E) is applied in the emergency phase as a survey management tool. It is based on an improved version of the procedure proposed in (Notti et al., 2023b), to obtain a first assessment map of the area affected by PL in the aftermath of the rainfall event, immediately available for survey field operations and risk management. The second phase is post-emergency mapping (PANDA-PE), in which the PL inventory is progressively improved with the availability of new images and ancillary data (*e.g.*, high-resolution DTMs, field survey information, UAV surveys), of which acquisition is usually arranged in the stages immediately following the event. The availability of progressively more detailed and higher-resolution data, allows the initial mapping to be refined, identifying the false positive and resolving the eventual gap of cloud cover of the first map. The PANDA-PE aims to obtain a reliable inventory tool for the subsequent phase of validation, risk mitigation and action planning.

The proposed methodology was applied both in the emergency and post-emergency phases in a portion of northeastern Apennine chain (Central Italy) to map the dramatic consequences of two severe rainfall events that occurred in May 2023. The maps obtained were also validated by a third-party (Ferrario, 2023) manual inventory made on high-resolution satellite images.

2. Study area

2.1. Geological and geomorphological settings

The study area covers the central-eastern sector of the Tuscan-Emilian Apennines, within the provinces of Bologna, Ravenna, and Forlì-Cesena, Emilia-Romagna Region, and a small portion of the Tuscany Region (Florence Province) (Fig. 1). The area of interest (AOI) was identified as the mountainous and hilly regions predominantly impacted by the dual rainfall occurrences in May 2023 and was pinpointed with a particular focus on the sector where the second event (16–17 May) recorded precipitation exceeding 150 mm or the cumulative rainfall of two events surpassed 250 mm (Fig. 2b).

This territory pertaining to the Tuscan-Emilian Apennine segment is mainly characterized by a mountainous to hilly morphology, with elevations ranging from 1300 m a.s.l. in the Apennine portion to 50 m a.s.l. towards the Po Plain. This Apennine sector, a fold and thrust belt, is mainly constituted by turbiditic deposits (flysch) with the alternation of mudstone and massive rocks as sandstones and calcarenites (Pini, 1999) (Fig. 1b). Considering the high-medium slope values and the presence of lithologies prone to erosion, this territory is extremely susceptible to slope instabilities. According to the IFFI catalogue (Trigila et al., 2008) the most widespread landslide typologies are earth flows, translational/rotational slides and complex landslides, generally triggered by snow melting and moderate but exceptionally prolonged (even up to 6 months) periods of rainfalls. On the other hand, shallow landslides and debris flows are generally less prevalent; however, their occurrence rapidly increases during high-intensity rainfalls or by prolonged low-intensity rainfalls (Benedetti et al., 2005; Ibsen and Casagli, (2004); Martelloni et al., 2013; Martina et al., 2010). This territory generally displays a high degree of urbanization characterized by numerous small inhabited areas scattered in the hilly zones connected with the main urban centers by a dense road and rail network. Consequently, geohazard related to landslides is one of the major issues affecting the entire Region.

2.2. The rainfall events

During May 2023, an extended portion of the Central Apennine, specifically the Emilian Apennine side and the Po Plain of the Emilia-Romagna Region, was affected by two consecutive rainstorms that occurred in less than twenty days: i) 1-3th May 2023 weather event, and ii) 16–17 May 2023 weather event (Brath et al., 2023).

In the first event, a low-pressure area generated a convergence of moist air, interacting with the Apennine chain in the central-eastern sector of the Region (*i.e.*, provinces of Bologna, Ravenna and Forlì-Cesena), and a small portion of the Tuscany Region included in the Adriatic river basins (Reno and Lamone). Referring to the spatial gridded data (5 km of spatial resolution) of rainfall available on the SIMC platform (https://dati-simc.arpae.it/opendata/erg5v2/timeseries/mappa.html), this first event led to rainfall accumulations in the hilly area even exceeding 200 mm (Arpae-SIMC, 2023a), in the central area (cells ID 1628, ID 1505 Fig. 2a) and 150 mm in the western limit (cell ID 1302) calculated on the whole event (about 40 continuous hours). The average hourly intensity ranged from 3 to 6 mm/h, with some peaks up to 10 mm/h (Fig. 2a). This event was weaker in the eastern part with cumulated rainfall of 75 mm (cell ID 2031, Fig. 2b). Other minor rainfall events contributed up to 50 mm of rainfall between the two events in the same area.

In the second event, a cyclone transiting the Mediterranean affected approximately the same area impacted by the previous event, with peak rainfall slightly shifted to the east (*i.e.*, provinces of Bologna and Forlì-Cesena). Most of the precipitations were concentrated in the central-eastern hills and foothills areas, with accumulations of ~ 250 mm in 35 h and peaks recorded during May 16 exceeding 200 mm (Arpae-SIMC, 2023b; Brath et al., 2023). The intensity of the second event was

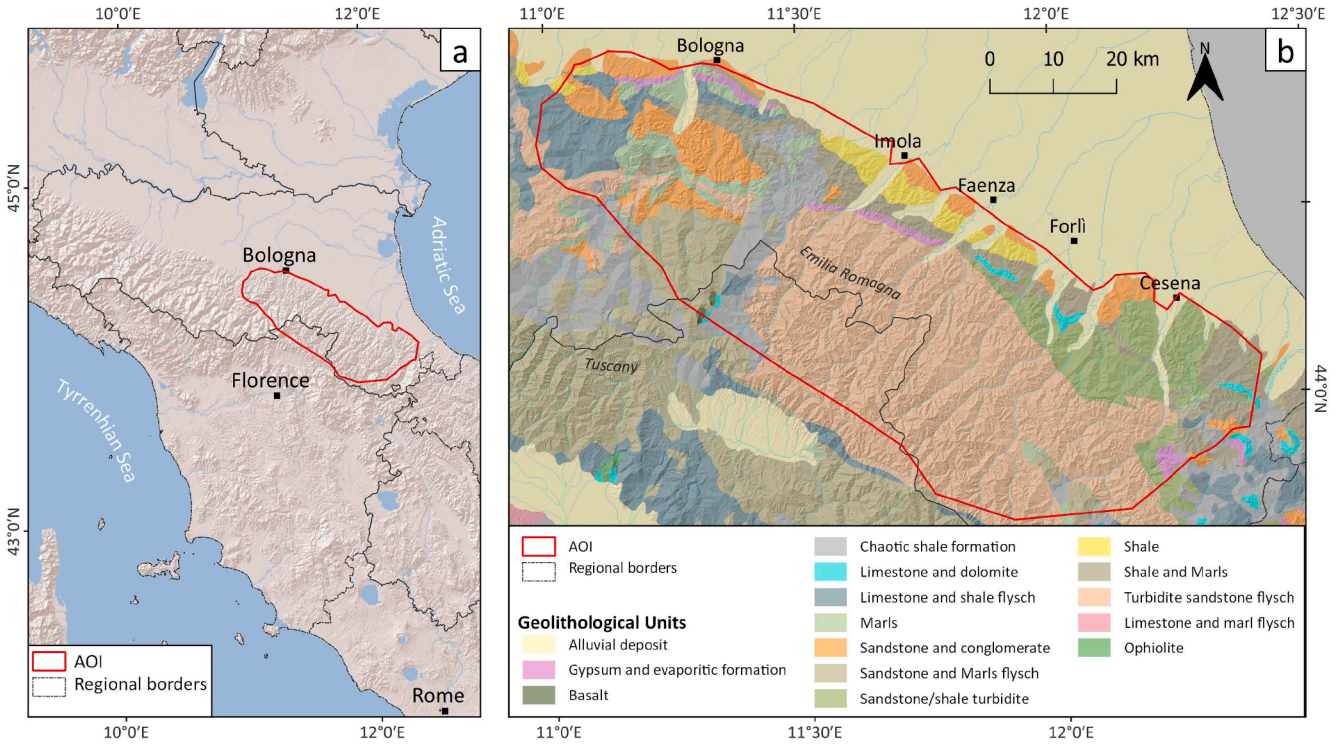

Fig. 1. (a) Location of the AOI that identifies the sector most affected by the rainstorm events that occurred in May 2023, and (b) simplified lithological map based on 1:500.000 scale lithological map of Italy (MASE, 2009).

also slightly higher than that of the first event, especially in the central-eastern part (7 mm/h), where some peaks reached 20 mm/h, especially in cell ID 2031(Fig. 2a).

These amounts of precipitation poured over an area close to saturation (according to the soil water index – SWI content available on Copernicus Global Land Service https://land.copernicus.eu/global/products/swi) by the intense rainfall events in the preceding days, making the soil unable to absorb part of the precipitations and triggering many shallow and deeper landslides.

3. Materials and methods

Following the methodological flow chart proposed in Fig. 3, we defined two main phases of PANDA approach for shallow landslide mapping:

- Emergency mapping (PANDA-E): It aims to create a first assessment map helpful for support in field surveys to estimate the most affected area in terms of landslide density and a preliminary estimate of damage. In this step, rapidity has priority on accuracy. The emergency mapping is based only on a semi-automatic methodology derived from Notti et al., (2023) that uses Sentinel-2 satellites.
- Post-Emergency mapping (PANDA-PE): This step aims to improve the first asset mapping and to make a more refined mapping of shallow landslides. This step could improve the semi-automatic methodology using the land use change filter and enhanced geomorphological filter. Here, high-resolution images from aerial or satellite can be used for validation. The mapping aims to create an accurate event map for research, land-use planning, or susceptibility studies.

It is not possible to quantify the time of the emergency phase, which may last from a few days up to several months, depending on many factors. For the Emilia case, we considered the emergency phase to have ended when the field survey for the first assessment and residual risk evaluation ended, approximately 40 days after the event.

3.1. The PANDA-E mapping steps and parameters

Performing a shallow landslide map over large areas during an emergency context, available immediately after a rainstorm event, requires a rapid and unsupervised mapping of the affected area. We implemented PANDA to obtain a prompt map of the ground effects based on free-cost optical satellite images.

The emergency methodology is based on those proposed by (Notti et al., 2023b), a GIS-based and user-friendly approach to map PLs, based on the difference between pre- and post-event Normalized Difference Vegetation Index (NDVI) obtained from satellite images, *e.g.*, free Sentinel-2 dataset, available on the Copernicus Dataspace Service (https://dataspace.copernicus.eu/) and geomorphological filtering. The variation in the NDVI ($NDVI_{var}$), mainly linked to the processes that occur during the rainstorm, allows the functional detection of surface changes and signs of PLs. Considering the emergency context, the need for images immediately following the event may result in some constraints in the post-event image selection. After a rainstorm, the availability of entirely could-free images can be challenging to achieve. However, if the cloud percentage is below an empirical threshold that allows an almost complete mapping (*e.g.*, <20 % of the study area), it is possible to exclude from PL mapping the areas covered by the clouds using the mask available on the Sentinel-2 dataset (Table 1), joined with a manual refinement to include cloud shadow. In our case, the first image was acquired on 23–05-2023, a week after the event, compared with the previous year image (13/05/2022). It is worth noting that The Google Earth Engine (GEE) platform has undergone advancements in cloud detection capabilities, enabling precise identification of both clouds and shadows (https://developers.google.com/earth-engine/tutorials/community/sentinel-2-s2cloudless).

Then, we combine two Boolean filters based on the $NDVI_{var}$ and slope gradient. The first one selected all the areas with an $NDVI_{var}$ below a certain threshold (based on visual evaluation of $NDVI_{var}$ pattern) that

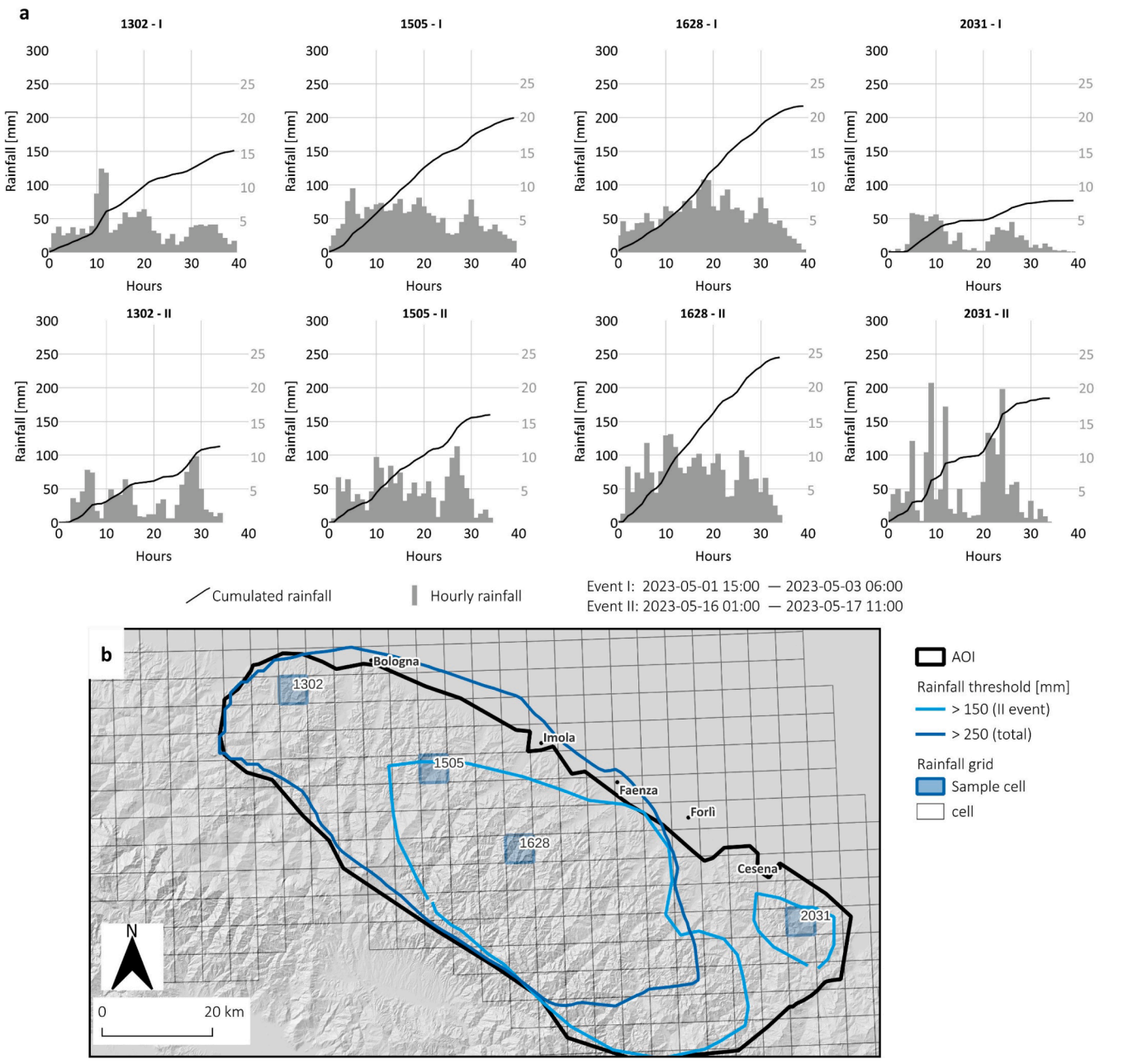

Fig. 2. Rainfall data of May 2023 events. a) Hourly (left Y-axis) and cumulated (right Y-axis) rainfall data (computed respectively for the May 1-3rd and the May 16-17th rainfall events. The precipitation time series utilized have been extrapolated from the grid of the SIMC platform (https://dati-simc.arpae.it/opendata/erg5v2/timeseries/mappa.html) over 4 representative cells. b) Location of selected cells and the rainfall contour lines used to delimit the AOI.

identify a PL. The second is a geomorphological filter based on slope gradient (derived from digital terrain model (DTM)). This filter is based on an empirical threshold (based on local geomorphology), below which an NDVI change is most likely unrelated to a shallow landslide occurrence. In the Boolean raster, the pixels where both thresholds are satisfied have a value of 1, and such pixels are extracted and converted into vectors: *i.e.* the PL polygons. In our study area, we used the thresholds $NDVI_{var}<=-0.3$ and slope $> 15°$. Such thresholds are empirically based on the pattern $NDVI_{var,}$ previous experience, the local geomorphological conditions, and literature (Ghorbanzadeh et al., 2022a; Notti et al., 2023b); such thresholds could be changed in iterative procedure in order to obtain the most likely ground truth scenario. In this case, we used a conservative $NDVI_{var}$ threshold for the problem related to cloud coverage.

In addition, the polygons have been intersected with the hydrographic network (polygon or buffered layer geometry) to exclude bank erosion processes or sediment deposition along the river system. The filtered polygons exemplify the area where a shallow landslide is most probably located. Consequently, the PL density map allows us to identify the most affected areas to focus emergency activities.

3.2. *The PANDA-PE steps and parameters*

After the preliminary release, in the post-emergency phase, it is possible to improve the PL database by acquiring new images and ancillary data. The aim is to obtain a more accurate mapping of the event impact and its consequences. Among the several improvements that can be made, the first is to use an utterly cloud-free image (cloud cover < 3 %) to have information on the whole AOI. In this case study, we found the first cloud-free image on 17 July 2023, compared with a pre-event

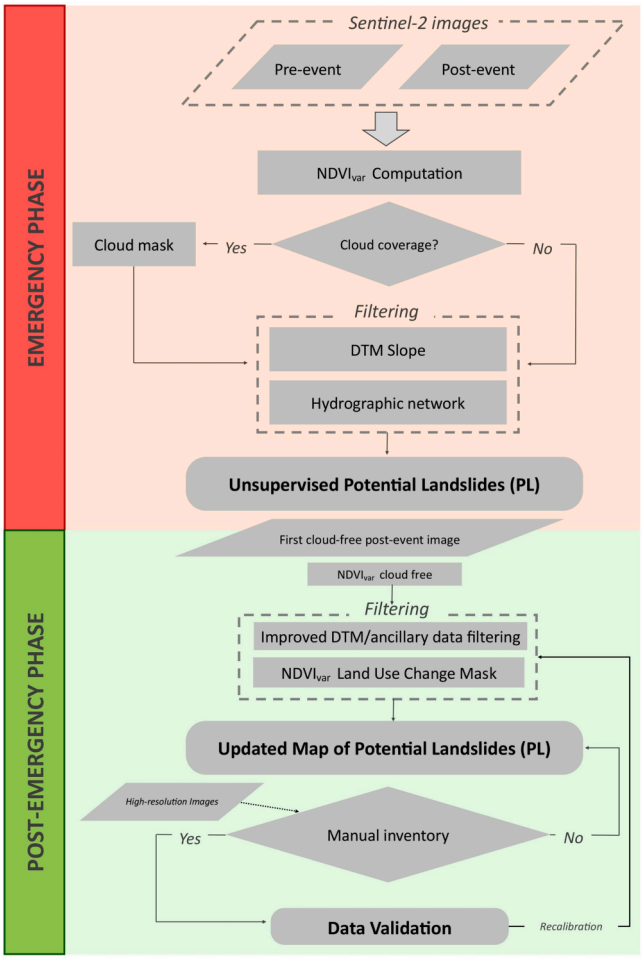

Fig. 3. The two-phase flowchart of PANDA methodology proposed for shallow landslide mapping.

Table 1
Used data for the shallow landslide mapping with PANDA-E and PANDA-PE steps related to the Emilia Romagna Rainstorm events.

		PANDA-E		PANDA-PE	
	Sensor and products	**pre-event**	**post-event**	**pre-event**	**post-event**
$NDVI_{var}$ for PL detection	Sentinel-2, Bottom-of-Atmosphere reflectance in cartographic geometry (L2A). B4, NIR (10 m)	13/05/2022	23/05/2023	22/07/2022	17/07/2023
	Cloud and shadow mask	Cloud probability mask available on the Sentinel-2 quality assessment folder (layer: MSK_CLDPRB_20m)		Cloud cover < 3 % cloud mask not necessary	
$NDVI_{var}$ filter for false positive related land-use change (LUC)	Sentinel-2, Bottom-of-Atmosphere reflectance in cartographic geometry (L2A). B4, NIR (10 m)	Not used		**pre-LUC** 17/02/2022	**post-LUC** 22/02/2023
Filtering	Slope derived from DTM	10 m DTM TIN Italy		5 m DTM Emila-Region	
	Hydrographic network	Available shapefile from Geoportale of Emilia-Romagna Region (https://geoportale.regione.emilia-romagna.it/download)			

image of 22 July 2022.

The false positive land use change (LUC) filter based on $NDVI_{var}$ is a second improvement. The change of land use, and vegetation activity, that intercurred between the pre-event images and the event is one of the leading causes of false positive (*e.g.*, a forest cut or change in crop cultivation). If available, a cloud-free image acquired slightly (*i.e.* in the same agricultural cycle) before the event can be compared with a synchronous image from the previous year. Leveraging the NDVI difference, it is possible to calculate a pre-event $NDVI_{var}$. If the mean LUC $NDVI_{var}$ in the PL is below an empirical threshold (<-0.15, in our AOI), we classify it as a possible false positive. In our case study, we could make this improvement only on a portion of the study area because the closest LUC image to the event (22–02-2023) features partial snow cover. The $NDVI_{var}$ LUC filter and cloud-free post-event images allowed us to use a less conservative threshold of $NDVI_{var}$ for PANDA-PE, which was fixed at −0.15.

Finally, the geomorphological filter could be improved from the emergency phase using a more detailed hydrographic network or slope-DTM. In our case study, a few months after the events, a 5 m DTM was available on the whole AOI and allowed us to improve the accuracy of the slope filter.

3.3. Comparison and validation with a manual inventory

In the aftermath of the May 2023 rainstorm, the authors conducted field surveys and rapid reports to aid regional and local authorities in identifying and mapping critical landslides. This allowed for testing the PANDA-E method, although on a limited scale, just a few days after the event. Moreover, we used data from geolocated reports, videos, and photos on the web to validate the first PANDA-E map locally.

Then, during the post-emergency phase, the results obtained from both methodology phases (*i.e.* PANDA-E and PANDA-PE) were validated by exploiting the manual landslide (ML) inventory made by Ferrario, 2023. This manual mapping, available on the Zenodo data repository, is based on Planet Scope satellite images (about 3 m of spatial resolution) published about 40 days after the event, overlapping most of our AOI (Ferrario and Livio, 2024). We also considered only the ML and PL with a median slope $\geq 15^{\circ}$ to make a homogeneous comparison and discard the process more related to the river erosion. We used the same validation schema described in (Notti et al., 2023b) where five intersection types are defined: True Positive (*i.e.* PL and ML complete overlapping), Partial Positive (*i.e.* PL that intersects a ML), False Positive (*i.e.* PL that not intersect or overlap a ML), Partial Detection (*i.e.* ML that intersect a PL) and False Negative (*i.e.* ML that not intersect or overlap a PL). We also calculate the statistics like the Detection Rate (DR) = (TP + PD)/(TP + PD + FN) and the False Positive Rate (FPR) = FP / (FP + TP + PP) and the standard performance of accuracy: precision (P) = TP / (TP + FP), recall R = TP / (TP + FN) and F_1score F_1 = 2TP / (2TP + FP + FN). For the Emilia-Romagna region, we also intersected the validation test with the land use dataset to evaluate the effect of land cover on the performance.

Additional local validation was made using the very-high-resolution (0.2 m) post-event images acquired by CGR S.p.A and available on the Emilia-Romagna Region web portal, specifically acquired for the 2023 rainfall events (https://geoportale.regione.emilia-romagna.it/approfondimenti/emergenza-maggio-23/emergenza-rer-maggio-2023-servizi).

4. Results

4.1. Application of PANDA-E

The PANDA method, used in the emergency related to the May 2023 Emilia-Romagna rainstorms, rapidly mapped potential ground effects in the aftermath of the second event. The unsupervised mapping of shallow landslides provided an overall territorial framework, that can be very useful for a first evaluation of the impact of the occurred event, the

distribution of damage and the definition of priorities in the scheduling of field activities (Notti et al., 2023a). The mapping of ground effects performed within the investigated areas revealed about 30,000 PLs (covering an area of 20 km^2, 0.5 % of the whole AOI), among them, a few thousand are most probably related to hydrological processes. About 10 % of PLs intersect the road network within 10 m. This map partially suffers from cloud cover affecting about 8 % of AOI (related to the available Sentinel-2 image acquired on 23rd May 2023), even if mainly in the southern portion of the observed area, close to the Adriatic-Tyrrhenian drainage divide, less affected by rainfall. Nevertheless, it is immediately possible to detect the sectors most affected by PL, on which to focus risk assessment and mitigation activities. Fig. 4a shows the Kernel density distribution of the PL centroid; the density was computed on a 100 m resolution grid with a search radius of km and uniform interpolation. It is possible to see that the zone featuring higher values (about 150 km^2) is nearby Modigliana municipality (more than 3000 PL) and matches rainfall data and ground evidence reported day-by-day by field operators during the emergency. The most affected municipalities, in terms of PL abundance and density, are reported in Table 2.

The histogram in Fig. 5 a shows the distribution of PL areas. Such distribution agrees with the power law distribution of shallow landslide areas (Bellugi et al., 2021; Guzzetti et al., 2002). Approximately 80 % of potential landslides (PL) exhibit sizes ranging from 100 m^2 (equivalent to one pixel of Sentinel-2) to 1000 m^2, as depicted in Fig. 5b. Some outlier values up to 1.2·105 m2 (Fig. 5 inset plot) are probably related to false positives due to the residual unfiltered cloud cover or land use and vegetation changes. Due to the spatial resolution of both Sentinel −2 and DTM, there are no PLs smaller than 100 m^2.

Because the first aim of the PANDA methodology is to rapidly detect the most affected area and the preliminary location of PL, it was almost impossible to validate it with a manual inventory, high-resolution images or extensive field surveys. However, leveraging the collected geolocated information and videos available on the web (*e.g.*, national newspapers or Localteam website https://www.localteam.it/), it was possible to carry out a local ground-truth comparison of PANDA results (Fig. 6 C-D). Moreover, during the field survey operated by our research group and started a few days after the event, several positive feedbacks were observed. For instance, Fig. 6 A-B shows a high correspondence between extrapolated PL polygons and phenomena observed.

Table 2
PL centroid density in the top 10 most affected municipalities.

Municipality	Inhabitants (dati.istat.it)	PL	PL Density (PL/km^2)	area affected (%)
Dovadola	1573	1708	43.6	3.17
Modigliana	4288	3717	36.6	2.32
Fontanelice	1913	907	24.4	1.87
Casola Valsenio	2498	2044	24.1	1.66
Predappio	6296	2010	22	1.38
Roncofreddo	3422	1125	22	1.31
Brisighella	7186	3551	18.4	1.12
Borgo Tossignano	3198	469	15.9	1.17
Civitella di Romagna	3639	1821	15.4	0.83
Mercato Saraceno	6797	1489	14.9	1.2

4.2. *The improved PANDA-PE inventory*

The improved PANDA-PE version was made in September 2023 (Fig. 7). The better quality of the post-event image, combined with the LUC filter and higher resolution DTM, allowed us to obtain a complete database of PL with about 54,000 polygons corresponding to an area of

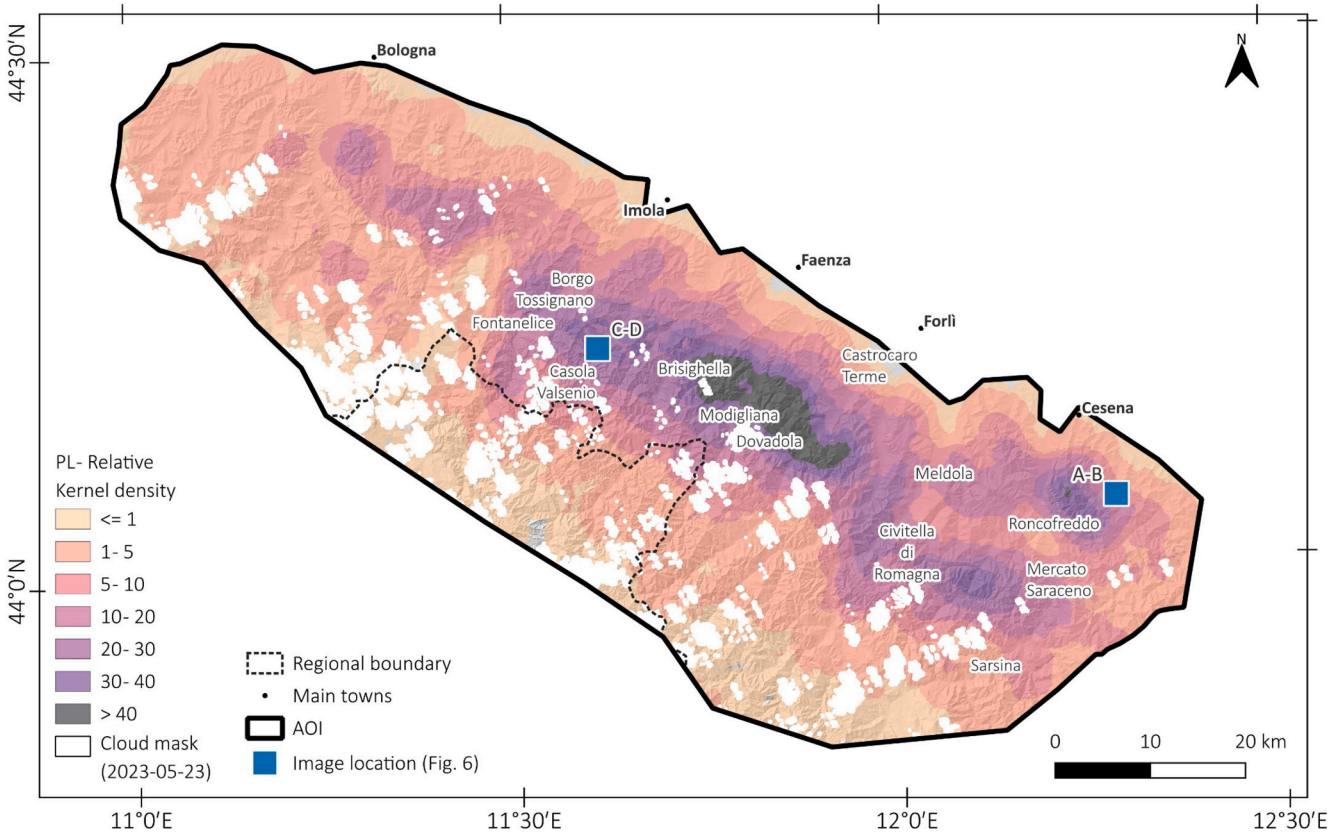

Fig. 4. The Kernel density map made with PL centroid (parameter: cell size 100 m; search radius 2.5 km; uniform interpolation; scaled) overlapped with the mask of cloud and shadow areas. The location of ground validation (Fig. 6) is also added to the same map.

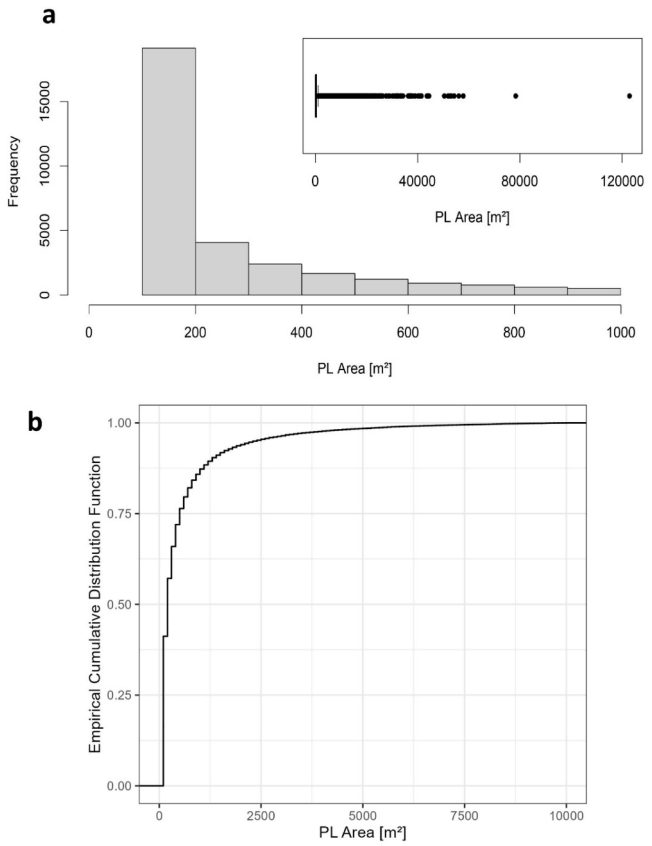

Fig. 5. A) histogram of pl area frequency distribution up to 1000 m2. Inset plot shows the whole distribution, including the outliers. b) Cumulative distribution, up to 10,000 m2.

about 40 km^2. The intersection with the hydrographic network allowed the classification of about 2700 polygons as a hydrological process, while the LUC NDVI$_{var}$ filter allowed the detection of about 1600 false positives (Fig. 7a). The relative Kernel density of the PL classified as shallow landside (Fig. 7b) shows a similar distribution of the PANDA inventory. In Fig. 7b, it is possible to observe the low density around rainfall cell ID 1505 and an isolated peak of PL density in correspondence with cell ID 2031, despite a similar amount of rainfall (Fig. 2).

Fig. 8 shows, over a test area, some details on the improvements of the PANDA-PE version. The higher resolution of 5 m DTM and derived slope (Fig. 8b) better identifies the critical slope than the previous 10 m resolution (Fig. 8a). Then, the NDVI$_{var}$ made with the post-event cloud-free image (2023–07-17) (Fig. 8c) and corrected with LUC NDVI$_{var}$ and hydrographic network layer (Fig. 8d) allowed the classification of the PL. The post-event high-resolution image of the Emilia-Romagna region (Fig. 8e) confirmed the validity of classification; in particular, the PLs classified as false positive with LUC NDVI$_{var}$ corresponds to a change in the cultivated field.

4.3. PANDA-PE PL density and distribution and correlation with rainfall, slope lithology and land use

Using the PANDA inventories, we made some rapid evaluations on the main factors that are commonly used in literature (Reichenbach et al., 2018) for shallow landslide distribution analysis or susceptibility modelling: the trigger factor (rainfall) and predisposal factors (slope, lithology and land use). The most interesting results are related to the triggering factor, the rainfall. We compared the PL density with rainfall distribution in Fig. 9 for the first event (panels a and a'), the second event (panels b and b'), and the summarized rainfall (panels c and c'). The rainfall and landslide density are calculated for each cell of the rainfall grid of the Emilia-Romagna region (SIMC platform https://dati-simc.arpae.it/opendata/erg5v2/timeseries/mappa.html). Panel b' of Fig. 9 shows a box plot of the PL density for each rainfall class of the second event (16–17th May 2023). It is important to note the relationship between cumulated rainfall and density, notably where the second event reached values up to 150 mm (300–400 mm, considering the cumulated precipitation of the two events). Conversely, the relation is less evident with the cumulated rainfall of the first event (Panel a' of Fig. 9). Most probably, while the first rainfall saturated the soil (https://land.copernicus.eu/global/products/swi) the second (also with high hourly intensity) triggered most of the processing. Moreover, the antecedent rainfall (see paragraph 2.2) also affected shallow landslide distribution. Considering the intensity-duration thresholds (Guzzetti et al., 2008; Mondini et al., 2023), both single and the combination of these two are above the trigger thresholds worldwide found. Compared to nearby historical events, the total rainfall of these two events (up to 500 mm and average intensity of 6 mm/h) is similar to the 2013 Marche events, while it is very different from the event that hit the nearby Marche region in September 2022 (Donnini et al., 2023), which showed much higher intensity and short duration.

As already known, the slope gradient is one of the main factors related to landslide distribution (Lee and Min, 2001). In our case, the landslide density related with the slope angle is a partial analysis, as we consider only a slope above 15° to extract the PL. Considering this there is a linear relationship between the percentage of the area affected by landslide and the slope angle, which ranges from 1 % for the with a slope between 15° and 20° up to 4 % for the area with slope gradient class 40°-45°.

The lithology also played a role in the distribution of shallow landslides density and distribution, with higher concentration in the arenaceous turbiditic unit, especially in the "Marnoso-Areaneacea formations". In contrast, shale and chaotic formations show less density of landslides. Considering the percentage of the area affected by landslides, the Marnoso-Areaneacea formations reach a peak of 20 Kernel Density against the 4 KD of chaotic shale. The lithology has a strong influence on the slope degree distribution. The lithology also explains some incongruency with rainfall distribution: for instance, the low PL density (KD 8) of cell ID 1505 with cumulated rainfall of 350 mm located in chaotic shale, by contrast, the higher PL density (KD 15) of cell ID 2031 in arenaceous turbiditic formation with low rainfall (170 mm). The role of lithology in landslide density was already documented in the nearby Marche 2022 event (Donnini et al., 2023).

The land use (based on the 2020 Land cover database of Emilia-Romagna Region, 2023) already influences the landslide density distribution but less reliably compared to the previous factors because the methodology introduces possible bias in this comparison. For instance, the higher PL density on oak-hornbeam and chestnut forest types is related to the fact that this type of land use is located mainly on the arenaceous turbiditic formation and in the area most affected by rainfall. Meanwhile, beech forests in the southern limit of the study area, which are less affected by rainfall, show low PL density. At the same time, the distribution of PL shallow landslides may suffer an underestimation detection bias in the area where the vegetation cover is already lower (vineyard, badland), or an overestimation where human activity interferes with vegetation (cultivated land), as already reported in previous work (Notti et al., 2023a) and in paragraph 5.2.

5. Discussions

5.1. PANDA-E mapping time and accuracy

During the emergency phase, like in the Emilia-Romagna event, it is crucial to quickly establish an overall framework for the most affected areas. An important point to stress here is that, due to the relevant emergency occurred, the rapid mapping refers to the ground variation. The obtained product does not correspond to a geomorphological

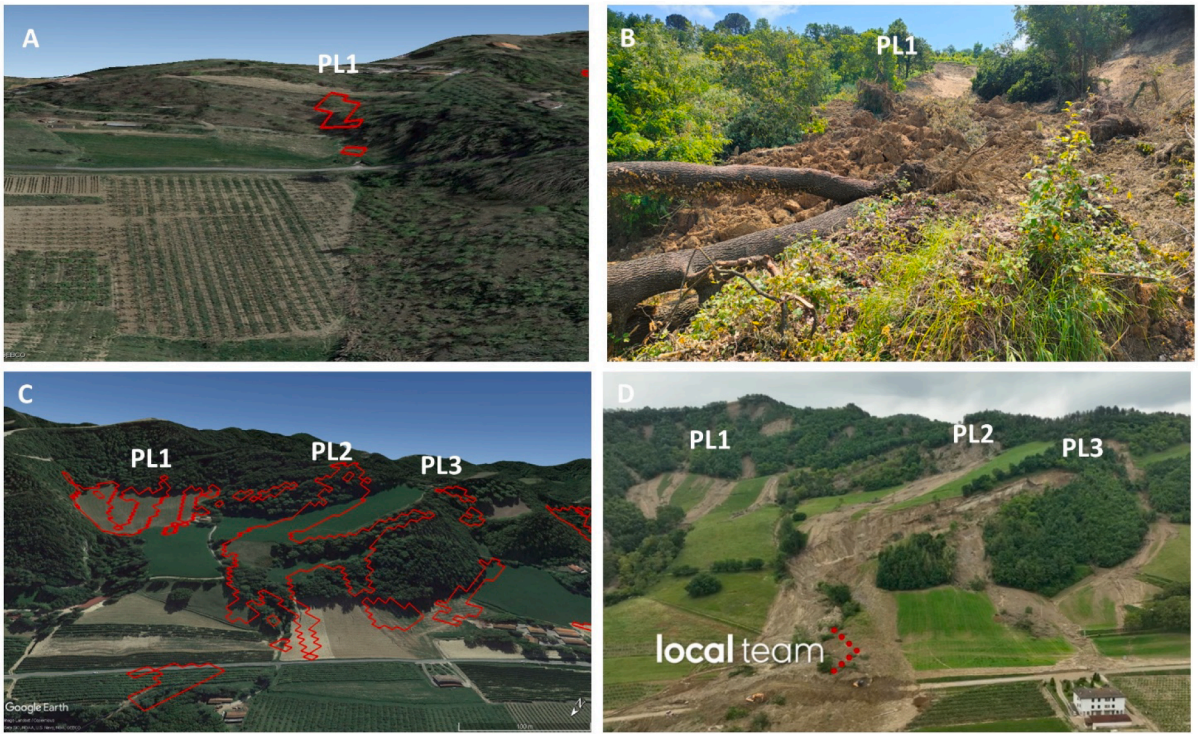

Fig. 6. Comparison between the potential landslide polygons overlapped to Google Earth Satellite images and the on-field observations and web-based images or videos. Montiano municipality, Forlì-Cesena Province, affected by a rotational sliding evolved in an earth flow: A) PL overlapped to Google Earth pre-event image (13/09/2022 Credit ©Maxar, 2022); B) Post-event ground photo taken a few days after the events (Credit Davide Notti). SP306 close to Casola Valsenio hamlet, Ravenna, affected by several shallow landslides along the upstream slope: C) PL overlapped to Google Earth pre-event image (13/09/2022 Credit ©Maxar, 2022); D) Same PL on the frame from Localteam video ().
Source: https://www.localteam.it/video/grandi-frane-a-casola-valsenio-la-collina-appare-sventrata

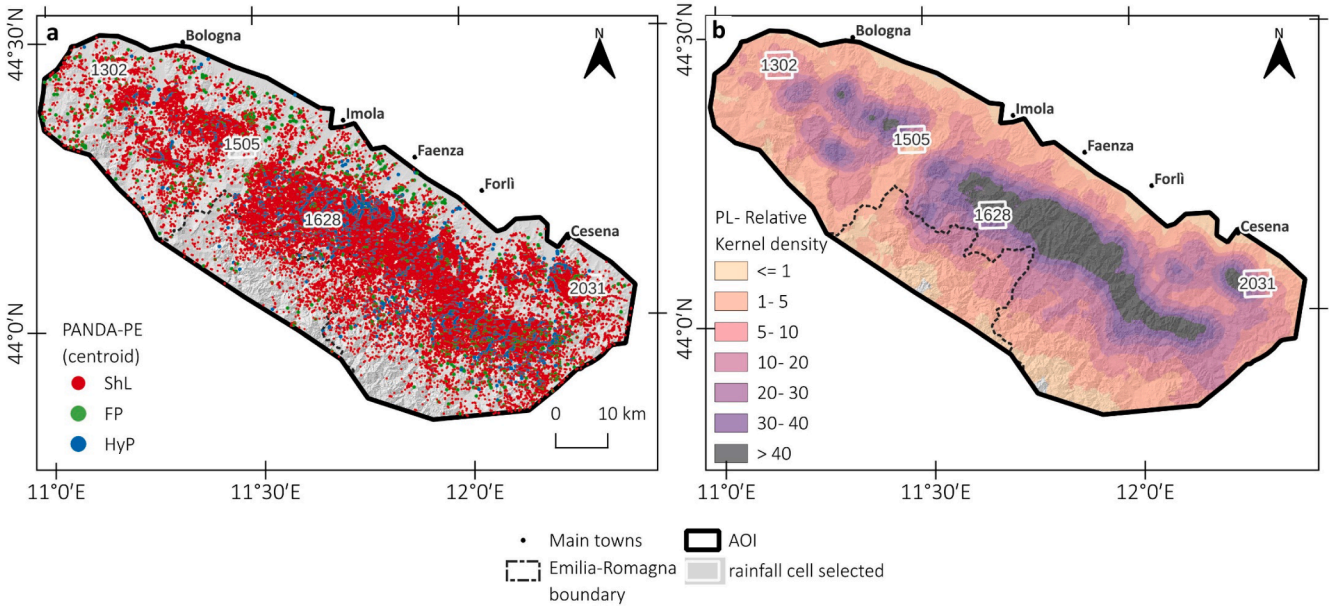

Fig. 7. A) the centroids of improved panda-pe pl classified in a shallow landslide (shl), hydrological process (hyp) and false positive related land-use changes (fp); b) relative kernel density (parameter: cell size 100 m; search radius 2.5 km; uniform interpolation; output value scaling: scaled) of PL classified shallow landside, associated to the selected cells used in Fig. 3 for analysis of rainfall events.

landslide inventory in the strict sense because it is the output of a semi-automatic feature extraction based on middle-resolution images. Consequently, the proposed approach may generate potential false-positive cases mainly related to land use changes during the observed period (*e.g.*, cultivation areas) or the effect of cloud cover. The semi-automatic cloud filter allows the partial reduction of false positives. However, local residual effects related to cloud coverage remain at this early stage. Another limitation is related to the spatial resolution and

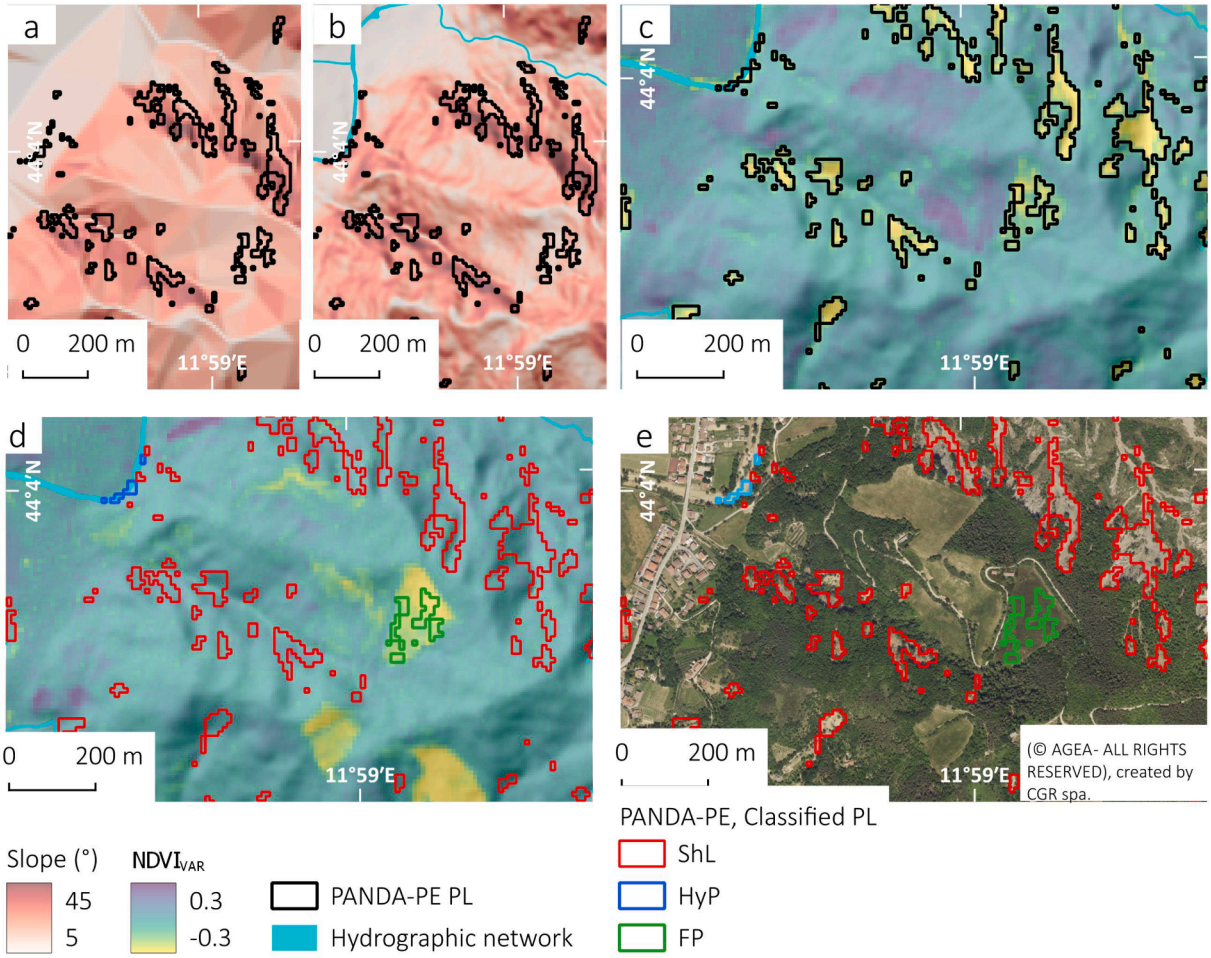

Fig. 8. PANDA-PE PL overlapped to: a) 10 m spatial resolution slope-DTM; b) 5 m spatial resolution slope-DTM. c) PANDA-PE PL overlapped to cloud-free $NDVI_{var;}$ d) Classified PANDA-PE - PL overlapped to LUC $NDVI_{var;}$ and hydrographic network, e) Classified PL overlapped to post-event high-resolution images.

accuracy of the DTM, which hamper the slope filtering. Despite the above limits, the obtained map provides a tool, freely and immediately available after a catastrophic event, useful for the field survey operations devoted to residual risk assessment. The use of Sentinel-2 satellite images allows to a totally free-of-charge approach, ensuring a cost-effective and user-friendly downloading and management with a free cloud computing platform as Google Earth Engine. Nevertheless, PANDA is structured to operate with any optical spaceborne imagery, regardless of revisiting time or resolution. However, the exploitation of satellite images with shorter revisit times, like PlanetScope, is, in any case, inherently constrained by cloud coverage, particularly after a rainstorm event. Surely, higher-resolution sensors improve detection accuracy in terms of landslide boundaries and extent, but generally have costs not affordable for several users, misaligning with the objectives of PANDA. Leveraging on the "Open Data Program" (https://www.maxar.com/open-data), a comparative analysis of potential shallow landslides mapped using Sentinel-2 and Maxar data (0.5 m resolution) has been carried out. The availability of Maxar imagery, limited to the flooded areas, did not allow extensive analysis over the hilly area, which was only sporadically covered by the available imagery. The comparison displayed, as the resolution increases, an improved accuracy and quality of mapping, but, excluding those exceptional cases of data availability, they commonly entail a related cost. Conversely, the PANDA methodology aims to be a free and user-friendly tool for timely use immediately after a calamitous event, to identify occurred landslides in terms of number and density. While the reduced time to generate the ground effects map might compromise the accuracy of landslide outlines compared to high-resolution imagery, it still offers valuable support for initial emergency response actions. The first draft map obtained was generated on 26th May 2023, just three days after the Sentinel-2 acquisition and after one week, the map was published on the Zenodo repository. The need to have such an instrument within a few days, immediately after a rainstorm, obviously precludes the possibility of a large-scale data validation with a manual landslide inventory. A manual mapping on high-resolution images or by field survey operations requires, on such a large area, several weeks/months of work or many operators (Galli et al., 2007; Milledge et al., 2022), an incompatible timing during the emergency phase. In the case of the May 2023 events, the first manual inventory was produced about one month after the event and released in vector format in the Zenodo repository (Ferrario, 2023), and a technical report, including a landslide map, was produced about six months later (Brath et al., 2023). Directly comparing the accuracy, time, and cost of this study methodology to others is complicated or even biased due to variations in study area size and event intensity, as well as the aim of the final users of the method. However, some insights can be gleaned. For example, Mondini et al., (2011) spent five days creating and validating their inventory, with two experts in remote sensing and geomorphology, using PCA, covering an area of 9.4 km^2. PANDA could potentially reduce processing and validation time by two days for larger areas, and it does not need remote sensing expertise, but at the cost of lower accuracy. In agreement with PANDA also Mondini et al., (2013) found that the use of a limited number of morphometric parameters (*e.g.,* slope and hydrographic network) reduces the complexity of the classification framework and the computation time.

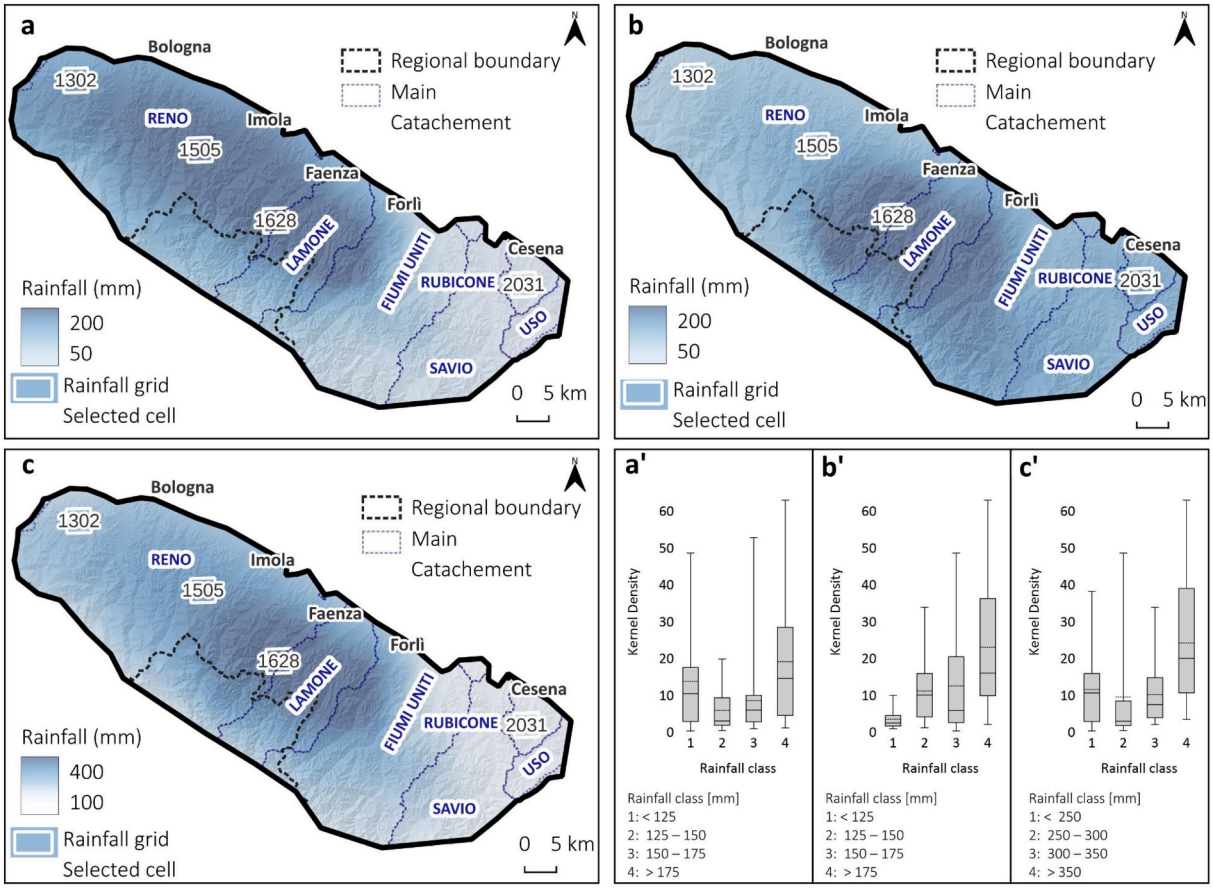

Fig. 9. Maps of interpolated rainfall distribution and associated bar plots of PL Kernel Density for rainfall class respectively for: the 1 – 3rd May rainfall event (a and a'), 16 – 17th May rainfall event (b and b') and the sum of the two events (c and c'). The Kernel Density and rainfall are computed on the rainfall grid of SIMC platform (https://dati-simc.arpae.it/opendata/erg5v2/timeseries/mappa.html).

(Li et al., 2016), compared simple change detection with more sophisticated techniques that improve results. In this work, using geomorphological filters and LUC in the post-emergency phase could improve the performance, avoiding expertise in processing. Similarly, Lu et al., (2019) demonstrated the effectiveness of PCA in small forested areas using Landsat-8 and Sentinel-2 data compared to NDVI variation. However, their study area was small and required remote sensing expertise. Compared to the other approaches, PANDA provides some important advantages, ensuring a methodology capables to process wide areas in a short time (*e.g.*, two days for Sentinel-2 scene), with a reduced number of input data, commonly available worldwide, that are needed to run the model (NDVI, cloud cover, slope, hydrographic network), through a GIS-based procedure completely cost-free and suitable for users with different degree of experience.

5.2. Comparison and validation with a manual inventory. PANDA-E vs PANDA-PE

As shown in Notti et al., (2023b) the PL dataset could be validated with manual-based landslide inventory (ML) to evaluate its accuracy. In the emergency phase, finding data for validation is almost impossible, except from local cases such as reports or geolocated video (Fig. 6). In the weeks following the event, it could be possible to obtain or create a manual inventory based on different sources (*e.g.*, satellite, aerial, ground-based).

The PANDA-E PL inventories made during the Emergency (v 1.0) phase and the improved PANDA-PE (v 2.0) version were validated using the manual inventory made by Ferrario, (2023), available on the Zenodo data repository. The overall results for the validation study area are resumed in Table 3. It is possible to observe that the improved PL inventory (PANDA-PE) increased the surface of detected shallow landslides about two times (7.6 to 13.4 km^2) with a slight decrease of False Positive (11.3 to 10.9 km^2) more evident in percentage (24 % to 18 %). The overall performances of PL inventories calculated as reported in paragraph 3.3 are compared in Table 4. Fig. 10 shows, on a test area, a comparison between the validation of PANDA-E (Fig. 10a) and the PANDA-PE (Fig. 10b). It is possible to observe the improvement of the PANDA-PE PL version, considering the area: the overall F_1-score increased from 0.40 to 0.59, which is a satisfactory result, considering the complex land use. Considering the validation test only for broadleaf forest land-use type, the F_1-score reached a value of 0.72 (Fig. 10c), similar to studies that use high-resolution images (Meena et al., 2023) or tested in tropical forests land-use (Ghorbanzadeh et al., 2022a), or with more complex multi-sensor analysis (Lu et al., 2019) On the other hand, the F_1 value decreased to 0.15 on cultivated land (Fig. 10e) also urban areas and badlands show lower performance. The effect of land use on

Table 3
Intersection cases summary with ML inventory (Ferrario, 2023) by polygon count and total area for the whole AOI.

PL Inventory version	**PANDA-E**		**PANDA-PE**	
Intersection case	Polygon N	Area Km^2	Polygon N	Area Km^2
True Positive (TP)	20,230	7.6	30,224	13.4
Partial Positive (PP)	16,534	3.0	24,598	15.3
False Positive (FP)	11,329	11.3	28,871	10.9
Partial Detection (PD)	14,704	13.8	24,449	11.5
False Negative (FN)	24,482	11.4	13,750	8.0
Total	87,279	47.1	121,892	59.1

Table 4
Performance of PL inventories considering the area compared to ML inventory (Ferrario, 2023).

Parameters	PANDA-E	PANDA-PE
DR	65 %	76 %
FPR	52 %	28 %
Precision	40 %	55 %
Recall	40 %	62 %
F_1-Score	0.40	0.59

landslide detection performance has also been observed in other studies (Dias et al., 2023; Mondini et al., 2011). In areas with low vegetation, the use of stereoscopic or 3D data is found to be the most effective solution (Fiorucci et al., 2018). A possible solution could be to use SAR amplitude images; however, this requires a complex process, and they could be partially affected by the geometry distortion related to topography. For instance, to map shallow landslides in a forested area in Hokkaido, Japan, Nava et al., (2022) obtained a score of 0.61 using INSAR with U-NET methods, while from the same research group, Meena et al. (2023) in the same area, using optical data of Planet and U-Net and f1 score of 0.81. Moreover In the same area, using SAR, it was noticed the effect of land use on performance detection (Jung and Yun, 2020; Mondini et al., 2021).

It was possible to verify that most FNs are related to shallow landslides smaller than 100 m^2, an intrinsic limit related to Sentinel-2 spatial resolution (10 m) and the badland area (Fig. 10d), especially in the marl-shale formation. As mentioned before, FPs correspond to land use changes not detected by the LUC filter because they occurred later in the image used for LUC $NDVI_{var}$ (2023–02-22) or were located in an area covered by snow. By random checking on the very high-resolution images of CGR, we also noted that in several cases, some FP were correctly detected, most probably because of some cloud cover, and lower resolution (3 m vs 0.2 m) of the Planet images used for ML inventory. On the other hand, as reported by (Ferrario, 2023) manual inventory could also be affected by the false negative and false positive errors that influence the comparison. Finally, validation using high-resolution images also allowed the detection of some cases in which the PANDA-E performed better than PANDA-PE, where, for instance, the accumulation material was removed (along the main roads) or was interested in the regrowth of herbaceous vegetation occurring from May to July (*e.g.*, the small landslides in or the north sector of Fig. 10a and Fig. 10b).

6. Conclusions

The primary purpose of the PANDA is to serve as an initial and swift emergency assessment map, allowing users to identify the most heavily impacted areas. It has shown reliability, particularly in quickly mapping large areas with cost-free inputs, leveraging a user-friendly processing.

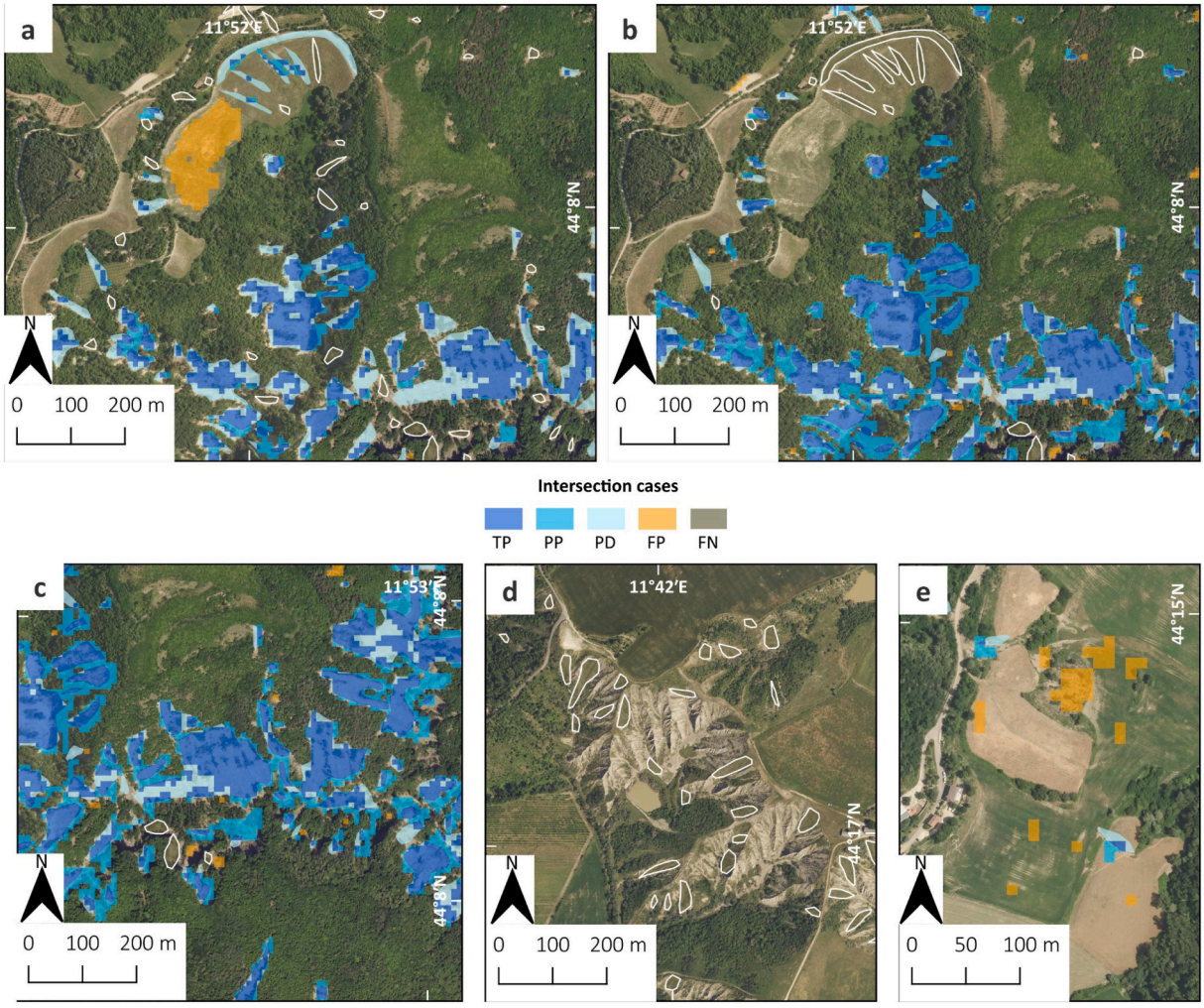

Fig. 10. A detail over a test area of the validation of PL Inventories: a) PANDA-E; b) PANDA-PE improved inventory. The performance of PANDA-PE mapping depends on land use: c) broadleaf forest shows best performance; d) shallow landslides on badlands are rarely detected (False Negative); e) cultivated land still produces False Positive, despite filtering. The post-event high-resolution post-event images created by CGR spa (© AGEA - ALL RIGHTS RESERVED).

PANDA in emergency phase, applied to the May 2023 rainfall events of northeastern Apennine, allowed us to map, in a few days after the event and at a low-cost, tens of thousands of PL over a wide area (>4000 km2) and identified the most affected sector (about 150 km2) where PL density reached values up to 50 km2.The whole map was immediately shared on a public data repository to be used and improved by the expert community. The obtained PL inventory was tested directly during the emergency field surveys with positive feedback. In contrast, emergency rapid mapping is limited by the possibility of having a completely cloud-free image, increasing the probability of false positives. Such limitations during the post-emergency mapping (PANDA-PE) can be partially solved by improving PL using a cloud-free image, a high-resolution slope-DTM and a land use change filter also based on NDVI variation, thus decreasing False Positive and increasing inventory accuracy as confirmed by validation employing an independent manual inventory (F1-score improved 0.4 to 0.59). The performance of the semi-automatic mapping based on NDVI is related to land use, working well on vegetated areas, and worse on bare soils and cultivated land, and this should be considered in emergency and post-emergency mapping. Potential enhancements to the PANDA methodology may involve refining the filtering capabilities to address cloud cover and variations in land use. Moreover, the conversion of the proposed methodologies into a software would make PANDA a user-friendly tool accessible for everyone. Overall, this application confirmed the suitability of the PANDA methodology for shallow landslide detection in several contexts worldwide. The enhanced PANDA-PE methodology further refines landslide inventory accuracy, paving the way for improved disaster management strategies.

CRediT authorship contribution statement

Davide Notti: Writing – original draft, Formal analysis, Data curation. **Martina Cignetti:** Writing – original draft, Methodology, Formal analysis, Data curation. **Danilo Godone:** Writing – review & editing, Validation, Data curation. **Davide Cardone:** Writing – original draft, Formal analysis, Data curation. **Daniele Giordan:** Writing – review & editing.

Declaration of competing interest

The authors declare that they have no known competing financial interests or personal relationships that could have appeared to influence the work reported in this paper.

Data availability

Data are available at the link https://zenodo.org/records/10706716.

Acknowledgements

We thank the two anonymous reviewers for their comments and suggestions that greatly improved the quality of the paper.

References

Arpae-SIMC, L'evento meteo-idrogeologico del 1–4 Maggio 2023 (technical analysis related to the weather, hydrogeological and hydraulic event) 2023 Agenzia Regionale per la Protezione Ambientale Emilia-Romagna.

Arpae-SIMC, L'evento meteo-idrogeologico e idraulico del 16–18 Maggio 2023 (technical analysis related to the weather, hydrogeological and hydraulic event) 2023 Agenzia Regionale per la Protezione Ambientale Emilia-Romagna.

Bellugi, D.G., Milledge, D.G., Cuffey, K.M., Dietrich, W.E., Larsen, L.G., 2021. Controls on the Size Distributions of Shallow Landslides. Proceedings of the National Academy of Sciences. https://doi.org/10.1073/pnas.2021855118/-/DCSupplemental.y.

Benedetti, A.I., Casagli, N., Dapporto, S., Palmieri, M., Zinoni, F., 2005. Modello statistico per la previsione operative dei fenomeni franosi nella regione Emilia-Romagna. Ital. J. Geosci. 124, 333–344.

Bessette-Kirton, E.K., Coe, J.A., Schulz, W.H., Cerovski-Darriau, C., Einbund, M.M., 1950. Mobility characteristics of debris slides and flows triggered by hurricane Maria in Puerto Rico. Hungr Evans. https://doi.org/10.1007/s10346-020-01445-z.

Bordoni, M., Persichillo, M.G., Meisina, C., Crema, S., Cavalli, M., Bartelletti, C., Galanti, Y., Barsanti, M., Giannecchini, R., D'Amato Avanzi, G., 2018. Estimation of the susceptibility of a road network to shallow landslides with the integration of the sediment connectivity. Nat. Hazards Earth Syst. Sci. 18 (6), 1735–1758. https://doi.org/10.5194/nhess-18-1735-2018.

Brardinoni, F., Slaymaker, O., Hassan, M.A., 2003. Landslide inventory in a rugged forested watershed: a comparison between air-photo and field survey data. Geomorphology 54, 179–196. https://doi.org/10.1016/S0169-555X(02)00355-0.

A. Brath N. Casagli M. Marani P. Mercogliano R. Motta Rapporto Della Commissione Tecnico-Scientifica Istituita Con Deliberazione Della Giunta Regionale n 2023 Region Emila Romagna Bologna (Italy).

Casagli, N., Cigna, F., Bianchini, S., Hölbling, D., Füreder, P., Righini, G., Del Conte, S., Friedl, B., Schneiderbauer, S., Iasio, C., Vlcko, J., 2016. Landslide mapping and monitoring by using radar and optical remote sensing: Examples from the EC-FP7 project SAFER. Remote Sens. Appl. Soc. Environ. 4, 92–108. https://doi.org/10.1016/j.rsase.2016.07.001.

Casagli, N., Frodella, W., Morelli, S., Tofani, V., Ciampalini, A., Intrieri, E., Raspini, F., Rossi, G., Tanteri, L., Lu, P., 2017. Spaceborne, UAV and ground-based remote sensing techniques for landslide mapping, monitoring and early warning. Geoenvironmental Disasters 4, 9. https://doi.org/10.1186/s40677-017-0073-1.

Cignetti, M., Godone, D., Giordan, D., 2019. Shallow landslide susceptibility, Rupinaro catchment, Liguria (northwestern Italy). J. Maps 15 (2), 333–345. https://doi.org/10.1080/17445647.2019.1593252.

Corominas, J., van Westen, C., Frattini, P., Cascini, L., Malet, J.P., Fotopoulou, S., Catani, F., Van Den Eeckhaut, M., Mavrouli, O., Agliardi, F., Pitilakis, K., 2014. Recommendations for the quantitative analysis of landslide risk. Bull. Eng. Geol. Environ 73, 209–263. https://doi.org/10.1007/s10064-013-0538-8.

Dias, H.C., Hölbling, D., Grohmann, C.H., 2023. Rainfall-induced shallow landslide recognition and transferability using object-based image analysis in Brazil. Remote Sens. 15, 5137. https://doi.org/10.3390/rs15215137.

Doan, V.L., Nguyen, B.-Q.-V., Pham, H.T., Nguyen, C.C., Nguyen, C.T., 2023. Effect of time-variant NDVI on landside susceptibility: a case study in Quang Ngai province, Vietnam. Open Geosci. 15 https://doi.org/10.1515/geo-2022-0550.

Donnini, M., Santangelo, M., Gariano, S.L., Bucci, F., Peruccacci, S., Alvioli, M., Althuwaynee, O., Ardizzone, F., Bianchi, C., Bornaetxea, T., Brunetti, M.T., 2023. Landslides triggered by an extraordinary rainfall event in Central Italy on September 15, 2022. Landslides 20 (10), 2199–2211. https://doi.org/10.1007/s10346-023-02109-4.

Drusch, M., Del Bello, U., Carlier, S., Colin, O., Fernandez, V., Gascon, F., Hoersch, B., Isola, C., Laberinti, P., Martimort, P., Meygret, A., Spoto, F., Sy, O., Marchese, F., Bargellini, P., 2012. Sentinel-2: ESA's optical high-resolution Mission for GMES operational Services. Remote Sens. Environ. 120, 25–36. https://doi.org/10.1016/j.rse.2011.11.026.

Đurić, D., Mladenović, A., Pešić-Georgiadis, M., Marjanović, M., Abolmasov, B., 2017. Using multiresolution and multitemporal satellite data for post-disaster landslide inventory in the republic of Serbia. Landslides 14, 1467–1482. https://doi.org/10.1007/s10346-017-0847-2.

Ferrario, M.F., Livio, F., 2024. Rapid mapping of landslides induced by heavy rainfall in the Emilia-Romagna (Italy) region in may 2023. Remote Sens. 16 https://doi.org/10.3390/rs16010122.

Ferrario, M.F., 2023. Inventory of landslides triggered by heavy rainfall in the Emilia-Romagna region (Italy) in May 2023. Doi: 10.5281/ZENODO.8102429.

Fiorucci, F., Giordan, D., Santangelo, M., Dutto, F., Rossi, M., Guzzetti, F., 2018. Criteria for the optimal selection of remote sensing optical images to map event landslides. Nat Hazards Earth Syst Sci 18, 405–417. https://doi.org/10.5194/nhess-18-405-2018.

Fiorucci, F., Ardizzone, F., Mondini, A.C., Viero, A., Guzzetti, F., 2019. Visual interpretation of stereoscopic NDVI satellite images to map rainfall-induced landslides. Landslides 16, 165–174. https://doi.org/10.1007/s10346-018-1069-y.

Galli, M., Ardizzone, F., Cardinali, M., Guzzetti, F., Reichenbach, P., 2007. Comparing Landslide Inventory Maps. Geomorphology. https://doi.org/10.1016/j.geomorph.2006.09.023.

Galli, M., Ardizzone, F., Cardinali, M., Guzzetti, F., Reichenbach, P., 2008. Comparing landslide inventory maps. Geomorphology, GIS Technology and Models for Assessing Landslide Hazard and Risk 94, 268–289. https://doi.org/10.1016/j.geomorph.2006.09.023.

Ghorbanzadeh, O., Crivellari, A., Ghamisi, P., Shahabi, H., Blaschke, T., 2021. A comprehensive transferability evaluation of U-net and ResU-net for landslide detection from Sentinel-2 data (case study areas from Taiwan, China, and Japan). Sci. Rep. 11, 14629. https://doi.org/10.1038/s41598-021-94190-9.

Ghorbanzadeh, O., Gholamnia, K., Ghamisi, P., 2022a. The application of ResU-net and OBIA for landslide detection from multi-temporal Sentinel-2 images. Big Earth Data 1–25. https://doi.org/10.1080/20964471.2022.2031544.

Ghorbanzadeh, O., Shahabi, H., Crivellari, A., Homayouni, S., Blaschke, T., Ghamisi, P., 2022b. Landslide detection using deep learning and object-based image analysis. Landslides 19, 929–939. https://doi.org/10.1007/S10346-021-01843-X/TABLES/2.

Giordan, D., Cignetti, M., Baldo, M., Godone, D., 2017. Relationship between man-made environment and slope stability: the case of 2014 rainfall events in the terraced landscape of the Liguria region (northwestern Italy). Geomat. Nat. Hazards Risk 8, 1833–1852. https://doi.org/10.1080/19475705.2017.1391129.

Giordan, D., Adams, M.S., Aicardi, I., Alicandro, M., Allasia, P., Baldo, M., De Berardinis, P., Dominici, D., Godone, D., Hobbs, P., Lechner, V., Niedzielski, T., Piras, M., Rotilio, M., Salvini, R., Segor, V., Sotier, B., Troilo, F., 2020. The use of unmanned aerial vehicles (UAVs) for engineering geology applications. Bull. Eng. Geol. Environ. 79, 3437–3481. https://doi.org/10.1007/s10064-020-01766-2.

Guzzetti, F., Malamud, B.D., Turcotte, D.L., Reichenbach, P., 2002. Power-law correlations of landslide areas in central Italy. Earth Planet. Sci. Lett. 195, 169–183. https://doi.org/10.1016/S0012-821X(01)00589-1.

Guzzetti, F., Cardinali, M., Reichenbach, P., Cipolla, F., Sebastiani, C., Galli, M., Salvati, P., 2004. Landslides triggered by the 23 november 2000 rainfall event in the Imperia Province, Western Liguria, Italy. Eng. Geol. 73, 229–245. https://doi.org/10.1016/j.enggeo.2004.01.006.

Guzzetti, F., Reichenbach, P., Cardinali, M., Galli, M., Ardizzone, F., 2005. Probabilistic landslide hazard assessment at the basin scale. Geomorphology 72, 272–299. https://doi.org/10.1016/j.geomorph.2005.06.002.

Guzzetti, F., Peruccacci, S., Rossi, M., Stark, C.P., 2008. The rainfall intensity–duration control of shallow landslides and debris flows: an update. Landslides 5, 3–17. https://doi.org/10.1007/s10346-007-0112-1.

Guzzetti, F., Mondini, A.C., Cardinali, M., Fiorucci, F., Santangelo, M., Chang, K.-T., 2012. Landslide inventory maps: new tools for an old problem. Earth Sci. Rev. 112, 42–66. https://doi.org/10.1016/j.earscirev.2012.02.001.

Ibsen, M.L., Casagli, N., 2004. Rainfall patterns and related landslide incidence in the Porretta-Vergato region, Italy. Landslides 1, 143–150. https://doi.org/10.1007/s10346-004-0018-0.

Jung, J., Yun, S.-H., 2020. Evaluation of coherent and incoherent landslide detection methods based on synthetic aperture Radar for rapid response: a case study for the 2018 Hokkaido landslides. Remote Sens. 12, 265. https://doi.org/10.3390/rs12020265.

Lee, S., Min, K., 2001. Statistical analysis of landslide susceptibility at yongin, Korea. Env Geol 40, 1095–1113. https://doi.org/10.1007/s002540100310.

Li, Z., Shi, W., Myint, S.W., Lu, P., Wang, Q., 2016. Semi-automated landslide inventory mapping from bitemporal aerial photographs using change detection and level set method. Remote Sens. Environ. 175, 215–230. https://doi.org/10.1016/j.rse.2016.01.003.

Lu, P., Qin, Y., Li, Z., Mondini, A.C., Casagli, N., 2019. Landslide mapping from multi-sensor data through improved change detection-based Markov random field. Remote Sens. Environ. 231, 111235 https://doi.org/10.1016/j.rse.2019.111235.

Martelloni, G., Segoni, S., Lagomarsino, D., Fanti, R., Catani, F., 2013. Snow accumulation/melting model (SAMM) for integrated use in regional scale landslide early warning systems. Hydrol. Earth Syst. Sci. 17, 1229–1240. https://doi.org/10.5194/HESS-17-1229-2013.

Martina, M., Pignone, S., Berti, M., Simoni, A., 2010. Un approccio bayesiano per individuare le soglie di innesco delle frane. In: Proceedings of the First Italian Workshop on Landslides.

MASE, 2009. Carta geolitologica d'Italia. Risoluzione 1:500.000.

Meena, S.R., Nava, L., Bhuyan, K., Puliero, S., Soares, L.P., Dias, H.C., Floris, M., Catani, F., 2023. HR-GLDD: a globally distributed dataset using generalized deep learning (DL) for rapid landslide mapping on high-resolution (HR) satellite imagery. Earth Syst. Sci. Data 15, 3283–3298. https://doi.org/10.5194/ESSD-15-3283-2023.

Milledge, D.G., Bellugi, D.G., Watt, J., Densmore, A.L., 2022. Automated determination of landslide locations after large trigger events: advantages and disadvantages compared to manual mapping. Nat. Hazards Earth Syst. Sci. 22 (2), 481–508. https://doi.org/10.5194/NHESS-22-481-2022.

Mondini, A.C., Guzzetti, F., Reichenbach, P., Rossi, M., Cardinali, M., Ardizzone, F., 2011. Semi-automatic recognition and mapping of rainfall induced shallow landslides using optical satellite images. Remote Sens. Environ. 115, 1743–1757. https://doi.org/10.1016/j.rse.2011.03.006.

Mondini, A.C., Marchesini, I., Rossi, M., Chang, K.-T., Pasquariello, G., Guzzetti, F., 2013. Bayesian framework for mapping and classifying shallow landslides exploiting remote sensing and topographic data. Geomorphology 201, 135–147. https://doi.org/10.1016/j.geomorph.2013.06.015.

Mondini, A.C., Guzzetti, F., Chang, K.T., Monserrat, O., Martha, T.R., Manconi, A., 2021. Landslide failures detection and mapping using synthetic aperture Radar: past, present and future. Earth-Sci. Rev. 216, 103574 https://doi.org/10.1016/J.EARSCIREV.2021.103574.

Mondini, A.C., Guzzetti, F., Melillo, M., 2023. Deep learning forecast of rainfall-induced shallow landslides. Nat. Commun. 14, 2466. https://doi.org/10.1038/s41467-023-38135-y.

Murillo-García, F.G., Alcántara-Ayala, I., Ardizzone, F., Cardinali, M., Fiourucci, F., Guzzetti, F., 2015. Satellite stereoscopic pair images of very high resolution: a step forward for the development of landslide inventories. Landslides 12, 277–291. https://doi.org/10.1007/s10346-014-0473-1.

Nava, L., Bhuyan, K., Meena, S.R., Monserrat, O., Catani, F., 2022. Rapid mapping of landslides on SAR data by attention U-net. Remote Sens. 14, 1449. https://doi.org/10.3390/rs14061449.

Notti, D., Cignetti, M., Godone, D., Giordan, D., 2023. Semi-automatic mapping of shallow landslides using free Sentinel-2 images and Google Earth engine. Nat. Hazards Earth Syst. Sci. 23, 2625–2648. https://doi.org/10.5194/NHESS-23-2625-2023.

Notti, D., Cignetti, M., Cardone, D., Godone, D., Giordan, D., 2023a. Rapid mapping of potential ground effects of the May 2023 Emilia-Romagna rainstorms. (Version 1).

Novellino, A., Pennington, C., Leeming, K., Taylor, S., Alvarez, I.G., McAllister, E., Arnhardt, C., Winson, A., 2024. Mapping landslides from space: a review. Landslides. https://doi.org/10.1007/s10346-024-02215-x.

Pini, G.A., 1999. Tectonosomes and olistostromes in the Argille Scagliose of the Northern Apennines, Italy, Vol. 335. Geological Society of America.

E.-R. Region 2020 - coperture vettoriali uso del suolo di dettaglio - edizione 2023 [WWW document] Geoportale. 2023 accessed 1.19.24 https://geoportale.regione.emilia-romagna.it/catalogo/dati-cartografici/pianificazione-e-catasto/uso-del-suolo/layer-14.

Reichenbach, P., Rossi, M., Malamud, B.D., Mihir, M., Guzzetti, F., 2018. A review of statistically-based landslide susceptibility models. Earth-Sci. Rev 180, 60–91. https://doi.org/10.1016/j.earscirev.2018.03.001.

Santangelo, M., Cardinali, M., Bucci, F., Fiorucci, F., Mondini, A.C., 2022. Exploring event landslide mapping using Sentinel-1 SAR backscatter products. Geomorphology 397, 108021. https://doi.org/10.1016/j.geomorph.2021.108021.

Santangelo, M., Marchesini, I., Bucci, F., Cardinali, M., Fiorucci, F., Guzzetti, F., 2015. An approach to reduce mapping errors in the production of landslide inventory maps. Nat. Hazards Earth Syst. Sci. 15 (9), 2111–2126. https://doi.org/10.5194/nhess-15-2111-2015.

Trigila, A., Iadanza, C., Spizzichino, D., 2008. IFFI project (italian landslide inventory) and risk assessment. First World Landslide Forum. 18–21.

van Westen, C.J., Castellanos, E., Kuriakose, S.L., 2008. Spatial data for landslide susceptibility, hazard, and vulnerability assessment: an overview. eng. geol. Landslide Susceptibility, Hazard and Risk Zoning for Land Use Planning 102, 112–131. https://doi.org/10.1016/j.enggeo.2008.03.010.